Edge transport studies in the edge and scrape-off layer of the National Spherical Torus Experiment with Langmuir probes

J. A. Boedo, J. R. Myra, S. Zweben, R. Maingi, R. J. Maqueda, V. A. Soukhanovskii, J. W. Ahn, J. Canik, N. Crocker, D. A. D'Ippolito, R. Bell, H. Kugel, B. Leblanc, L. A. Roquemore, D. L. Rudakov, and NSTX Team

Citation: Physics of Plasmas (1994-present) **21**, 042309 (2014); doi: 10.1063/1.4873390
View online: http://dx.doi.org/10.1063/1.4873390
View Table of Contents: http://scitation.aip.org/content/aip/journal/pop/21/4?ver=pdfcov
Published by the AIP Publishing

Edge transport studies in the edge and scrape-off layer of the National Spherical Torus Experiment with Langmuir probes

J. A. Boedo,[1,a)] J. R. Myra,[2] S. Zweben,[3] R. Maingi,[3] R. J. Maqueda,[3] V. A. Soukhanovskii,[4] J. W. Ahn,[5] J. Canik,[5] N. Crocker,[6] D. A. D'Ippolito,[2] R. Bell,[3] H. Kugel,[3] B. Leblanc,[3] L. A. Roquemore,[3] D. L. Rudakov,[1] and NSTX Team[3]
[1]*University of California San Diego, 9500 Gilman Dr., La Jolla, California 92093, USA*
[2]*Lodestar Research Corp, 2400 Central Ave., Boulder, Colorado 80301, USA*
[3]*Princeton University, PO Box 451, Princeton, New Jersey 08543, USA*
[4]*Lawrence Livermore National Laboratory, Livermore, California 94550, USA*
[5]*Oak Ridge National Laboratory, PO Box 2008, Oak Ridge, Tennessee 37830, USA*
[6]*University of California Los Angeles, PO Box 957099, Los Angeles, California 90095, USA*

(Received 19 December 2013; accepted 15 April 2014; published online 29 April 2014)

Transport and turbulence profiles were directly evaluated using probes for the first time in the edge and scrape-off layer (SOL) of NSTX [Ono *et al.*, Nucl. Fusion **40**, 557 (2000)] in low (L) and high (H) confinement, low power ($P_{in} \sim 1.3$ MW), beam-heated, lower single-null discharges. Radial turbulent particle fluxes peak near the last closed flux surface (LCFS) at $\approx 4 \times 10^{21}$ s^{-1} in L-mode and are suppressed to $\approx 0.2 \times 10^{21}$ s^{-1} in H mode (80%–90% lower) mostly due to a reduction in density fluctuation amplitude and of the phase between density and radial velocity fluctuations. The radial particle fluxes are consistent with particle inventory based on SOLPS fluid modeling. A strong intermittent component is identified. Hot, dense plasma filaments 4–10 cm in diameter, appear first ~2 cm inside the LCFS at a rate of $\sim 1 \times 10^{21}$ s^{-1} and leave that region with radial speeds of ~3–5 km/s, decaying as they travel through the SOL, while voids travel inward toward the core. Profiles of normalized fluctuations feature levels of 10% inside LCFS to ~150% at the LCFS and SOL. Once properly normalized, the intermittency in NSTX falls in similar electrostatic instability regimes as seen in other devices. The L-H transition causes a drop in the intermittent filaments velocity, amplitude and number in the SOL, resulting in reduced outward transport away from the edge and a less dense SOL. © *2014 AIP Publishing LLC*.
[http://dx.doi.org/10.1063/1.4873390]

I. INTRODUCTION

Work done in the last decades has shown that the observed particle and concomitant heat losses in the absence of, or in between, edge localized mode (ELM) pulses in the edge of tokamaks are due to electrostatic turbulence,[1–3] that seems to peak at/inside the edge. Much work supports the idea of the quenching of the turbulence by shear velocity breaking of turbulent eddies[4] that causes a transition to higher confinement dubbed H-mode,[5] which is considered the standard operation scenario for future devices. More recent research shows that scrape-off layer (SOL) density and temperature profiles in tokamaks and other devices are often close to exponential in the near SOL, but non-exponential and flat in the mid-far SOL[6] pointing to perpendicular transport in the mid-far SOL being much larger than previously thought. Intermittent, radial ballistic transport, mediated by plasma filaments[7–13] was identified as a vehicle for the enhanced radial transport and has been extensively documented in a wide range of devices. The main implication of this enhanced radial transport is an unexpected plasma-wall interaction and concomitant recycling and impurity release. Work on characterizing the transport, finding its origins and comparing it with numerical simulations has been performed in linear devices,[11,12] stellarators,[13–17] (Wendelstein W7-AS[13]), and tokamaks[17,19,20] (Alcator C-Mod,[21–25] DIII-D,[26–32] JT-60U,[33,34] ASDEX,[35] ASDEX-Upgrade,[36–38] JET,[39–42] CASTOR,[43] TCV,[44–46] NSTX,[47,48] MAST[49,50]) and stellarator-tokamak comparisons.[18] Its statistical properties have been examined[51,52] via the probability distribution function (PDF).[45,53,54] The intermittent objects are born in the vicinity of the last closed flux surface (LCFS) at the low field side (LFS) of the torus, as a result of interchange instability or other turbulence-generating mechanisms,[55–59] and move towards the wall due to $\nabla B \times B$ charge polarization and the resulting $E \times B$ radial drifts.[7,10]

Modeling of the tokamak edge plasmas[58–61] incorporating this transport has verified that under certain conditions plasma contact with the main chamber wall is significant, even when the distance to the wall is large compared with the density decay length existing at the separatrix. An extensive body of work imaging the edge of various devices with fast cameras[8,47,48] and beam emission spectroscopy (BES)[62] shows these objects as moving plasma filaments, elongated along the magnetic field lines.

Intermittent filaments, or "blobs," although fundamentally different from ELMs,[63,64] have similar dynamics once in the SOL,[42,65] appearing as long filaments travelling ballistically towards the wall with a flux dependent on density and radial velocity.[65–67] The intermittent filaments exist in both

a)Email: jboedo@ucsd.edu

L-mode and H-mode (albeit reduced) and are driven by broadband and interchange instabilities, whereas the ELMs are purely an H-mode phenomenon caused by peeling-ballooning instabilities that grow in the steep H-mode pedestal with a specific poloidal mode number, leading to larger filaments in the poloidal plane. ELMs, particularly type I, tend to affect the confinement of the pedestal region, and even the core by shedding up to 30% of the plasma energy into the SOL, whereas intermittent filaments appear at a high rate and contain relatively small amounts of plasma. Although these plasma filaments are generally not circular, but irregular, in the poloidal plane, assuming so allows for a reasonable, zero order size approximation.

As damage to the first wall elements and core plasma contamination with impurities in next-step fusion devices, such as ITER, should be prevented managing plasma interaction with the main chamber wall is of critical importance. Intermittent inter-ELM particle fluxes can exceed ELM-mediated fluxes in high-density, small ELM regimes,[67] and they become the main plasma-wall interaction mechanism in ELM-suppressed regimes.[68] Among critical questions for the future are: (1) What is the scaling of intermittency creation and transport with density/collisionality? (2) Is intermittency in spherical tokamaks similar to higher aspect ratio ones? (3) Can the spherical tokamak regimes help to improve models and their predictive power so that the intermittent transport in ITER-relevant regimes can be predicted or scaled?

We present data obtained by probes from the NSTX boundary contributing to these issues by characterizing the edge plasma profiles, the turbulence, transport, and the intermittency in L- and H-mode. We relate these measurements to global parameters and identify the instability regimes at play. We will show that the intermittency is present at the NSTX edge, where filaments are produced in the vicinity of the LCFS, leave the core ballistically at high speed (~3–5 km/s) with a radius of 4–10 cm, and propagate well beyond plasma-facing structures while decaying monotonically. We will also show how the aforementioned characteristics change upon entering H-mode. While some of these results provide an independent confirmation of earlier work in NSTX using the gas puff imaging (GPI) diagnostic,[47,48,92] others extend the analysis in ways not possible with GPI.

II. RESULTS

Experiments to characterize the NSTX edge and SOL, obtain fluctuation levels and statistics, and evaluate turbulent and intermittent transport were performed in four (two each) L-mode and H-mode discharges (plasma current, $I_p = 0.80$ MA, toroidal field, $B_T = 0.45$ T, injected power, $P_{in} = 1.3$ MW, safety factor, $q_{95} = 7$, discharge energy content, W = 50–70 kJ, plasma volume, $V_{Pl} = 11\,m^3$) as shown in Figs. 1(a)–1(f), in a diverted lower single-null (LSN) geometry, shown in Fig. 2. The density in NSTX rises monotonically, as seen in Fig. 1(a), in these discharges with boronized walls and no lithium, and the probe data were taken at roughly t ~ 0.28 s in all discharges, indicated in Fig. 1 by a dashed vertical line and a shaded box. The discharges have an identical current ramp-up and receive ~1.2 MW of neutral

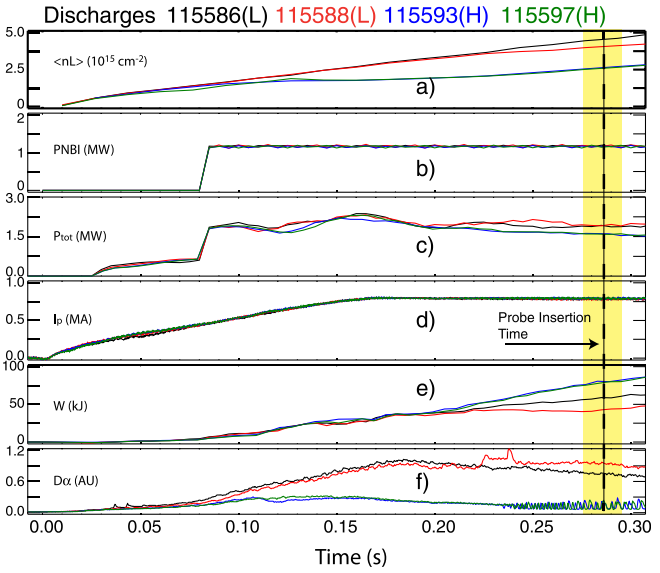

FIG. 1. Time evolution of four NBI-heated NSTX discharges, two in L-mode and two in H-mode. We show: (a) line-integrated density, (b) injected NBI power, (c) total input power (including ohmic), (d) discharge current, (e) discharge energy content, and (f) divertor D_α. Probe insertion time is roughly marked by a dashed vertical line at ~0.280 s.

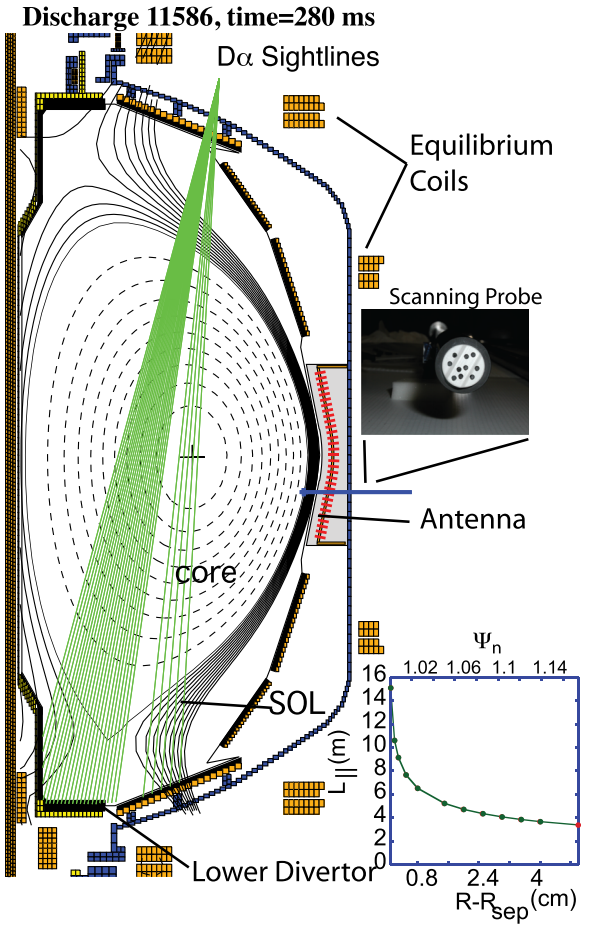

FIG. 2. Magnetic equilibrium for the LSN NSTX discharges considered, based in EFIT01, and showing the general magnetic topology, the D_α array, and scanning probe locations. The probe head is shown in upper inset, featuring 10 tips. Lower inset shows shortest connection length from the probe to the walls/divertor. The vessel is shown and also the equilibrium and OH coils, shown as arrays of small squares reflecting the conductor bundles.

beam injection (NBI) power at ~0.075 s that results in almost 2 MW of total input power, as seen in Figs. 1(b) and 1(c). The line-integrated discharge density in L/H mode at 0.28 s ranges from $5.0/2.0 \times 10^{15}$ cm^{-2}, shown in Fig. 1(a), corresponding to peak densities of $4.2/3.0 \times 10^{13}$ cm^{-3}, respectively. Peak electron temperatures reach 0.9/1.5 keV. Differences in the density evolution and divertor D_α are due to increased gas fueling to keep discharges in L-mode, and the presence of type III ELMs in H-mode that curb the density increase. A transition to an ELMy H-mode occurs in two of the discharges at ~0.24 s, followed by the presence of type III ELMs, seen in the lower divertor D_α signal, Fig. 1(f), detected via the imaging chords shown in Fig. 2.

Although many NSTX diagnostics are used, this work focuses on data from a fast scanning probe[69] located 18 cm below the midplane, shown in Fig. 2 as a horizontal bar. The probe head features 10 tips (Fig. 2 inset) that allow measurements of a wide range of plasma parameters with high spatial (1.5 mm) and temporal (1 μs) resolution, enabling turbulence/fluctuation measurements. Two of the tips, used as a swept double probe, provide T_e and n_e with 1 ms time resolution. The connection length from the probe to the nearest structures (Fig. 2 lower inset), quickly varies from ~16 m near the LCFS, to ~5 m in the near SOL, where it is connected to the lower divertor, and shortens further out as other structures appear.

The evolution of the probe position and saturation current, $I_{sat} = A_p 0.5 e n_e \sqrt{k_b(T_e + T_i)/m_i}$, signals are shown in Fig. 3(a) for an L-mode discharge as the probe moves from the far SOL and into the core. Data blocks 6 ms long are plotted in inserts [Figs. 3(b)–3(e)]. The I_{sat} signal shows high levels of intermittency throughout, even behind the stabilizing plates [Fig. 3(a)], reflecting the ballistic (i.e., convective or non-diffusive) character of the intermittent transport. The I_{sat} morphs from positive peaks in the SOL [Figs. 3(b)–3(d)] to voids inside the separatrix [Fig. 3(e)] as observed in DIII-D[9] and expected from an interchange-driven instability[56,57] and turbulent transport near marginal stability[70] models.

Profiles of electron temperature, T_e and density, n_e from the double probe (circles) and Thomsom scattering (TF squares), are shown in Fig. 4 for an L-mode discharge, demonstrating general good agreement between both diagnostics within error bars. The temperature and density are obtained from a four-parameter fitting $J = J_{sat} \times \tanh(eV_a/2k_bT_e)$ to the double probe characteristic[69] that is obtained every millisecond, assuming $T_e = T_i$, and resulting in a spatial resolution of ~1.0–1.3 mm. The measured density profiles are broad, almost flat, in the mid-far SOL and the high spatial resolution probe measurement clearly shows the location of structures in the far SOL (stabilizer plates and RF antenna) by a sharp drop at a normalized flux, $\psi_n \sim 1.3$ due to short connection lengths to the probe. The temperature profile shows more scatter, which is due to the strong intermittency and T_e being a sensitive function of the slope (i.e., a derivative) of the I–V characteristic. The strong turbulence in the SOL, considering that TS takes a snapshot and

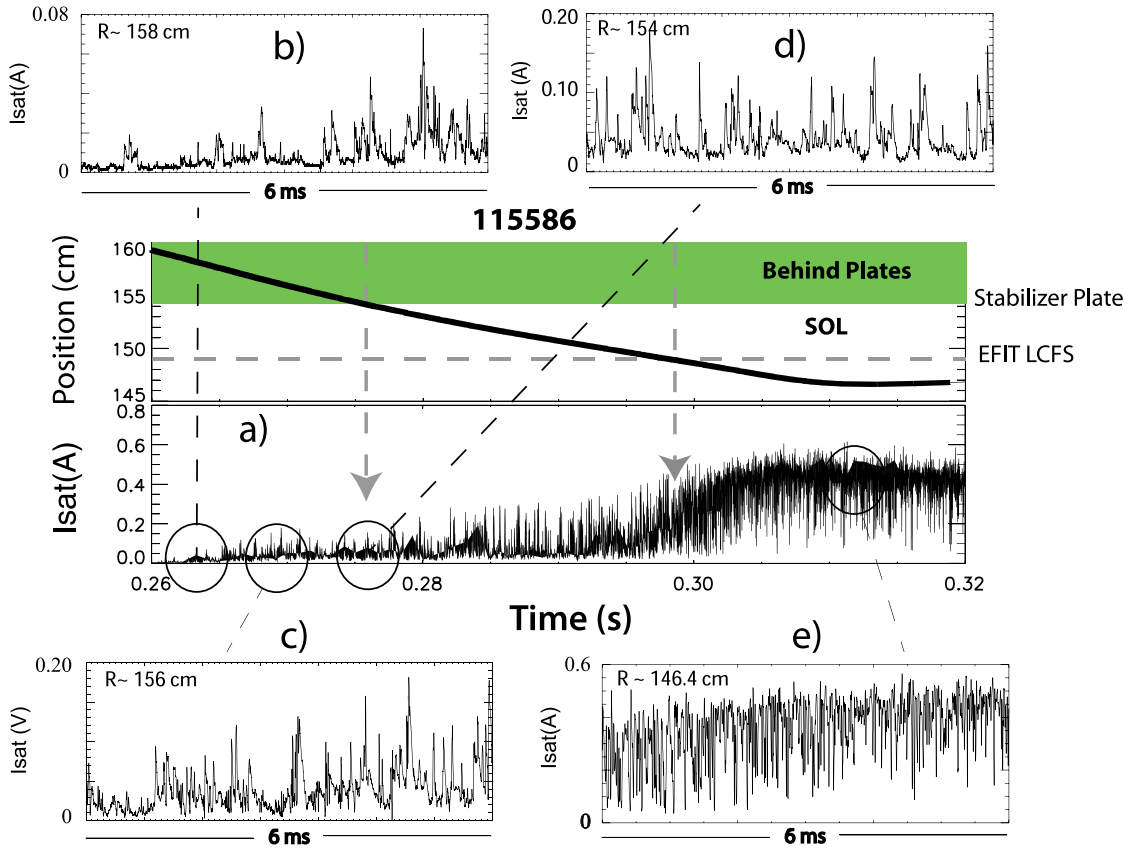

FIG. 3. I_{sat} trace from the scanning probe for a L-mode discharge correlating the signal to the various regions in the SOL and LCFS and showing how the intermittent character of the signal changes from peaks to voids in the core. The vertical arrows indicate when the probe crosses the stabilizing plates and the LCFS, respectively.

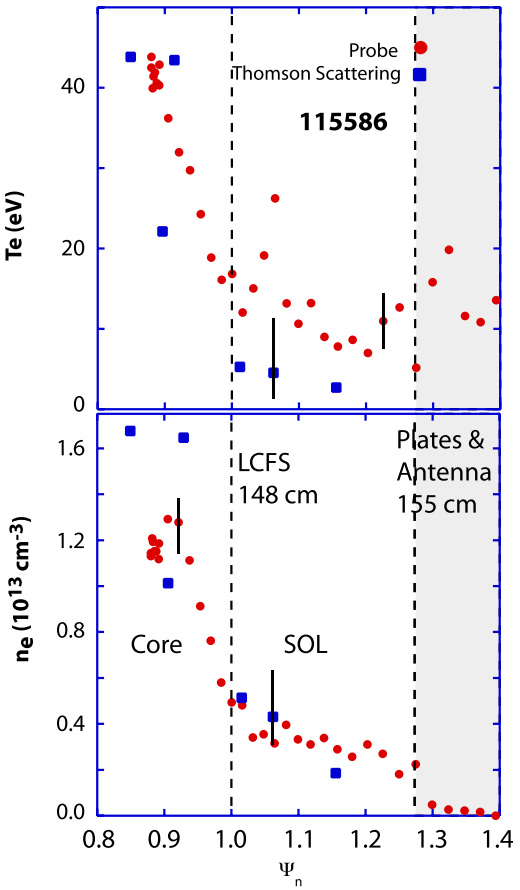

FIG. 4. n_e and T_e profiles from the scanning probe (circles) and Thomson scattering (squares) for an L-mode discharge. The positions of the core, LCFS, SOL, and far SOL structures (such as stabilizer plates and antenna) are clearly indicated.

the probe averages over 1 ms, also contributes to discrepancies between TS and probe data. In H-mode, ELMs are mostly filtered out of the T_e and n_e profiles since the I–V fitter often fails to converge during ELMs (i.e., there is no probe data point for the ELM time as the plasma is too transient during the 1 ms of the I–V characteristic to get fitter convergence). The mapping to flux coordinates is obtained by either running dedicated 2 ms time-resolution LRDFITs[71] or by interpolating existing EFIT[72,73] data (EFIT and LRDFIT are equilibrium reconstruction codes) to 1–2 ms resolution in order to accommodate the movement of the NSTX separatrix location.[69]

Profiles of saturation current density (i.e., tip current divided by tip area) are shown in Fig. 5 for all four of the (2) L- and (2) H-mode discharges to showcase discharge-to-discharge reproducibility and the importance of compensating for even small LCFS movements. The data show three main features: (1) the SOL becomes almost devoid of plasma in H-mode, (2) H-mode profiles "shift" further inside the EFIT LCFS, (3) H-mode profiles are steeper in the core, as expected, and (4) L-mode density is ~20× that of H-mode in the SOL.

The thick and flat SOL profiles in L-mode should correspond to more sizeable plasma-outer wall interaction (and wider divertor footprint) and should be concomitant with larger radial transport and fluctuation levels in comparison to H-mode. Therefore we have calculated the radial particle

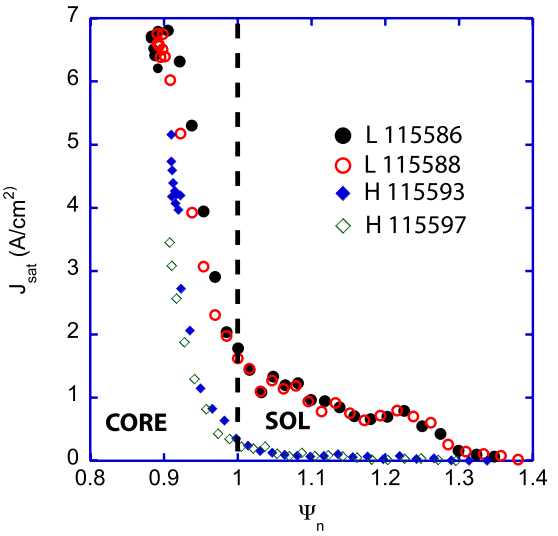

FIG. 5. Profiles of J_{sat} from the reciprocating probe for two H-mode (circles) and two otherwise similar L-mode (diamonds) discharges taken at the same time slice. The profiles feature excellent reproducibility. Dashed line indicates the EFIT01 separatrix.

flux density due to electrostatic fluctuations, as $\tilde{\Gamma}_r = \langle \tilde{n}\tilde{V}_r \rangle = \langle (\tilde{n}_e \tilde{E}_\perp)/|B| \rangle$, where $\tilde{E}_\perp$ is the fluctuating electric field perpendicular to the magnetic field B and the correlation is calculated over a 5 ms time series to obtain proper statistics without losing much spatial resolution. In extracting $\tilde{n}$ from $\tilde{J}_{sat}$we use the 1 ms time-resolved T_e obtained from the double probe in absence of a faster measurement, thus the effect of temperature fluctuations >1 kHz is ignored, although traditionally this is less than a 20% effect.[29]

We show profiles of $\tilde{E}_\perp$, $\tilde{n}$ and radial flux $\tilde{\Gamma}_r$ for two L- (circles), and two H-mode (diamonds) discharges in Figs. 6(a)–6(c) and the reproducibility is excellent within error bars, which are determined from statistical variation. The $\tilde{E}_\perp$ fluctuations [Fig. 6(a)] decay monotonically from the core towards the wall and, surprisingly, they are identical for L- and H-mode over the whole profile. The $\tilde{n}$ fluctuations [Fig. 6(b)], on the other hand, show much structure across the profile, peaking slightly inside the LCFS and dropping towards both the core and the SOL and are much lower (factor 2–10) in H-mode than in L-mode. The radial particle flux density, $\tilde{\Gamma}_r$, shown in Fig. 6(c) shows a spatial structure that somewhat reflects that of $\tilde{n}$ but featuring a larger gradient inside the LCFS, and showing a hint of a pinch, which indicates that $\tilde{n} - \tilde{E}_\perp$ cross phase effects[70] are extremely important in NSTX. There is a large difference between L- and H-mode flux densities, as expected; the L-mode flux peaks at $\sim 3\text{–}4 \times 10^{21}\ s^{-1}m^{-2}$ by the LCFS and remains large $(1\text{–}2 \times 10^{21}\ s^{-1}m^{-2})$ over a wide region of the SOL, whereas the H-mode flux density, peaks slightly inside the LCFS at $2.3 \times 10^{20}\ s^{-1}m^{-2}$ and is $\sim 1 \times 10^{20}\ s^{-1}m^{-2}$ throughout the SOL, a L/H factor of roughly 10 near the LCFS and of 20–50 or more in the SOL region. The large discrepancy between the profile behavior of the rms quantities and the flux density indicate strong cross-phase effects at play. L- and H-mode fluxes drop quickly inside the LCFS to negative values, a pinch, which has been suggested by Shats[75] to be the result of E_r shearing effects. The ensemble averaging of

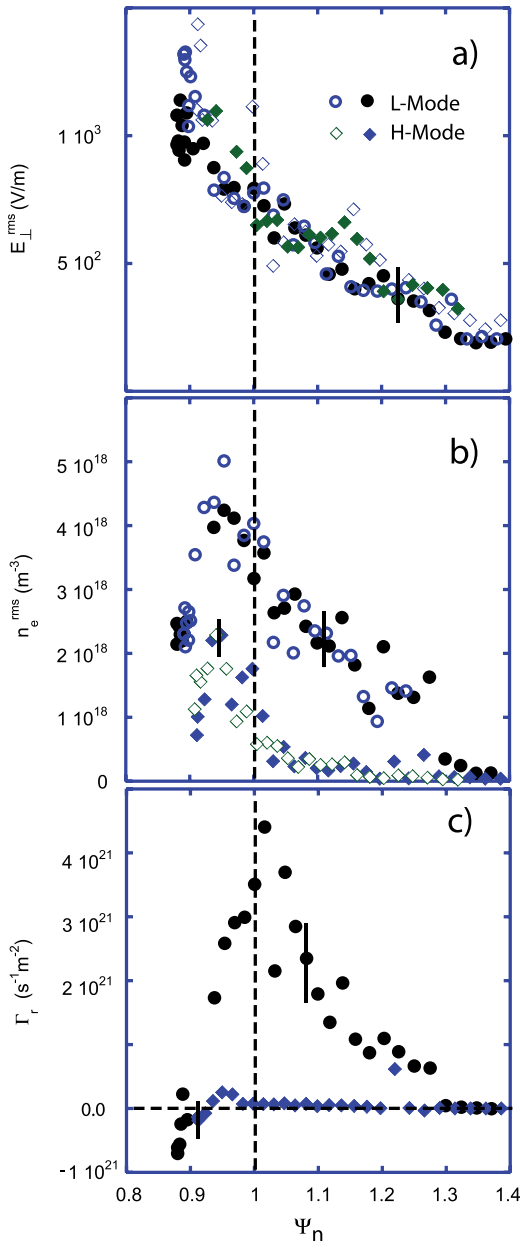

FIG. 6. Profiles of (a) rms levels of $E_\perp$, (b) rms levels of density fluctuations, and (c) turbulent radial particle transport, in H-mode (circles) and L-mode (diamonds) discharges. Dashed line indicates the EFIT separatrix.

5 ms used to calculate rms values and turbulent particle flux incorporates the effect of the type III ELMs, lasting $\leq$1 ms, in the H-mode cases, The ELMs can be clearly seen in the probe saturation current and floating potential (Fig. 7 top and middle) with higher time resolution and compared to the divertor D_α signal (Fig. 7 bottom) where delay and smearing effects (ion travel time to plates, plasma rotation and outgasing from the graphite) are evident.

The global particle flux crossing the separatrix has been estimated by running the SOLPS code[76] for these discharges. SOLPS uses a 2D fluid model of the plasma transport (the B2 code[77]), coupled to a Monte-Carlo neutral transport calculation of the recycled neutrals (the EIRENE code[78]) to calculate a plasma state consistent with the fueling due to particle recycling. Transport is assumed to be classical parallel to the magnetic field (with kinetic corrections), and

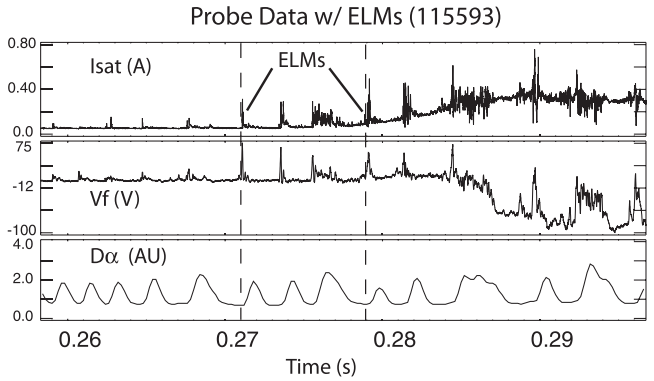

FIG. 7. Time evolution of (a) probe saturation current, I_{sat}, (b) floating potential, V_f, and (c) divertor D_α, during a probe plunge in a H-mode plasma. Type III ELMs can be clearly seen in the high time resolution probe signals, some are identified with vertical dashed lines, as well as inter-ELM turbulence. Time delay between probe and D_α signals is clear and due to various factors.

cross-field transport is governed by user-specified anomalous transport coefficients that are adjusted to reproduce the measured density and temperature profiles at the midplane. The power flowing into the simulated edge region and the fueling due to neutral beam injection and gas puffing that constrain the SOLPS simulations[79] are taken from the experimental values.

The measured peak D_α emission from the divertor has been reproduced in the simulation, indicating that the magnitude of the neutral recycling is captured in the code. Once SOLPS yields a plasma density and temperature spatial distribution that is reasonably similar to experiment (measured near the midplane), the neutral transport simulation within SOLPS can then be used to calculate the total ionization that occurs inside the separatrix. In steady state, this is equal to the total radial transport of ions across the separatrix. This method yields a total particle flux of $\approx 1 \times 10^{22}$ s^{-1} for the L-mode case $\approx 5 \times 10^{21}$ s^{-1} for the H-mode case. Using the probe data and a discharge area (according to EFIT01) of roughly 30 m^2, and assuming ***poloidally uniform*** turbulent fluxes, we obtain a L/H mode total flux ($\tilde{\Gamma}_r \times A$) of $\approx 1 \times 10^{23}/7 \times 10^{21}$ s^{-1}, an excellent fit in H-mode but discrepancy of almost a factor of 10 in L-mode. However, it is known the turbulent flux is more poloidally symmetric in H-mode while ballooning in character in the in L-mode[80,81] and highly peaked on the outer 25%–30% of the discharge surface area, in which case the L-mode data yield a total particle flux of $\approx 2.5 - 3.0 \times 10^{22}$ s^{-1}, in reasonable agreement with SOLPS global estimates and previous work[81] can be taken as a reaffirmation of the existence of ballooning-driven asymmetries in transport.

Normalized fluctuation levels of density, $\tilde{n}/\bar{n}$, and plasma potential, $\tilde{V}_{pl}/kT_e$, are shown in Fig. 8 for H-mode (open symbols) and L-mode (filled symbols). Normalized fluctuation levels for H- and L-mode are roughly 0.2 at $\Psi_n = 0.9$, rising quickly towards the LCFS, where the H-mode normalized density fluctuations, surprisingly, are larger by almost a factor of 2 at the LCFS than in H-mode. Normalized values and scatter in the SOL increase partly due to rapidly decreasing signal levels. Error bars are

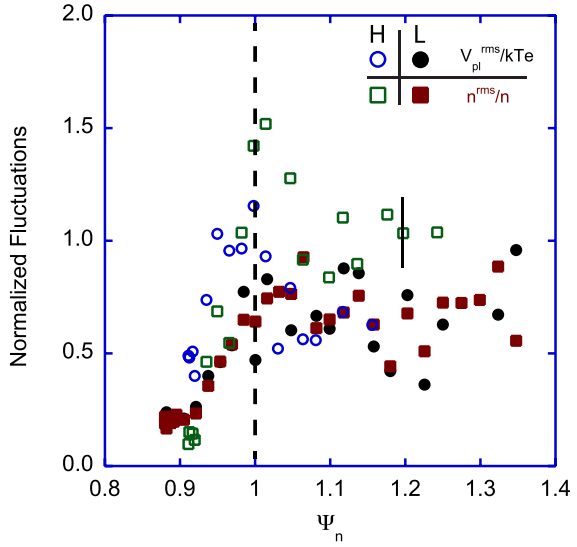

FIG. 8. Profiles of normalized plasma potential (V_{pl}^{rms}/kT_e) and density ($n^{rms}/\bar{n}$) fluctuation levels for L- (solid symbols) and H-mode (open symbols) discharges.

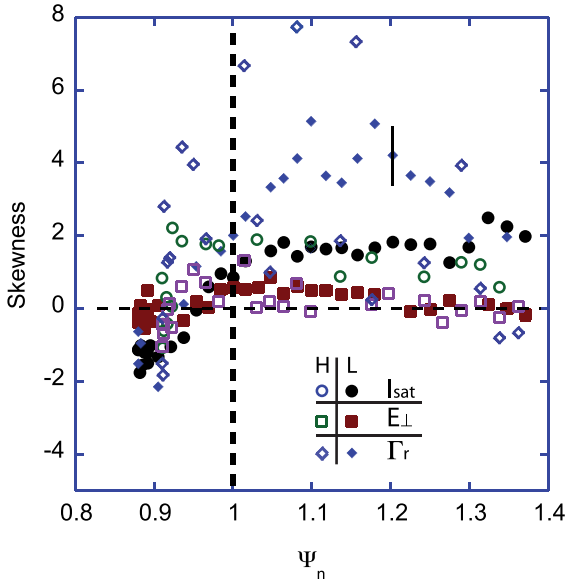

FIG. 9. Radial profiles of the Skewness of I_{sat}, $E_\perp$, and Γ_r fluctuations for otherwise similar L- (solid symbols) and H-mode (open symbols) discharges.

determined by statistical spread. Notice fluctuation levels at $\Psi_n \leq 0.9$ include not only peaks, but also voids.

Numerical simulations[82–90] and experiments[67,69,74,75,86,91] support the concept of turbulence born inside or at the LCFS[59] propagating into the SOL, in particular, interchange instability[83] seems to reproduce the general results. An element of these models is not only the production of bursts, but also the presence of density voids in the birth region of the intermittency, features that will cause a departure from a Gaussian distribution and is measurable via various statistical tools, such as skewness[39] of a signal

$$S = \sum_{i=1}^{N} (Y_i - \bar{Y})^3 / (N-1)\, s^3. \quad (1)$$

The skewness of various signals, I_{sat}, $E_\perp$ and Γ_r, is calculated and shown for L-mode (solid symbols) and H-mode (open symbols) in Fig. 9. The skewness reflects the presence of voids/peaks beyond a Gaussian distribution and that excess appears as negative or positive values[31] and thus it is clear from Fig. 9 that voids dominate for $\Psi_n \leq 0.95$, well inside the LCFS while peaks reign elsewhere. The data show that I_{sat} and Γ_r are highly skewed, whereas $E_\perp$ is less so. The high skewness of the flux, negative and positive, is understood as it compounds the non-Gaussian nature of both the density and electric field. The skewness is larger in H-mode than in L-mode for $\Psi_n \geq 0.95$ due to two factors: (1) the presence of ELMs and (2) a much smaller background plasma signal in H-mode (compared to the near-LCFS-produced filaments traveling through).

The peaks and voids can be separated from broadband turbulence and detailed information can be extracted via conditional averaging (CA)[39] of various quantities, using 4 or 5 ms time series and a 2.5× rms-level threshold criteria on the I_{sat} signal to extract the events (on I_{sat} and all other signals) that are then binned and accumulated on a 100 wide window (events are typically 10–20 μs long), as shown in Fig. 10. As a reminder, the CA process rejects the broadband turbulence and the events smaller than the 2.5× rms threshold, extracting the events at and above the threshold. In L-mode, a count of 20–50 events is customarily obtained in the 5 ms time series considered, resulting on a $\approx 1.0 \times 10^4\ s^{-1}$ production rate. We show the L-mode conditionally averaged, (open squares) and the related perpendicular electric field $E_\perp$, (solid circles) at 2.5 cm into the SOL in Fig. 10(a). Note that a radial velocity $V_r = E_\perp \times B/B^2$ of the plasma filament can be readily calculated from the $E_\perp$ signal and that there is a slight $\tilde{E}_\perp - \tilde{I}_{sat}$ de-phasing, as noted earlier on the time-averaged transport.

The conditionally averaged ***normalized*** I_{sat} signal binned on a 100 window is shown in Fig. 10(b) and the traces for various radial positions are superimposed to illustrate how the duration of the pulses change with radius. The development of a tail as the filaments propagate further into the SOL has been predicted in 2D simulations,[84–86] where the existence of an internal potential dipole produces a sheared double vortex structure compressing the density in front of the filament and dispersing it towards the back,[85] i.e., an interaction with the background plasma. The sheared flows can also lead to Kelvin-Helmholtz (KH) and other instabilities inside the filaments that can cause filament growth or dissipation. These data are very consistent with the 2D effects reported in the literature.[85,86]

The amplitude and event count of the peaks, $I_{sat}(+)$, and voids, $I_{sat}(-)$, in the I_{sat} signal from L-mode obtained from the CA process are shown vs radius in Figs. 11(a) and 11(b), respectively. The main vessel structures are indicated for reference and a polynomial fit was done (solid lines) to guide the eye. We can infer a filament production rate from Fig. 11(b) of $\sim 0.6 - 1 \times 10^4\ s^{-1}$ by tallying the number of events in a 5 ms time series used for conditional averaging. The (asymmetric) amplitude of both the positive and

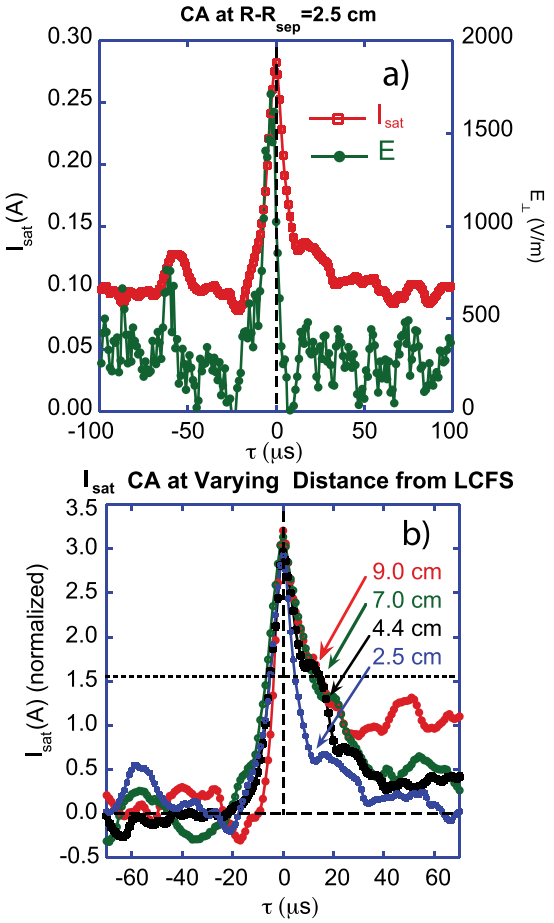

FIG. 10. Conditional averaging over 5 ms of: (a) the I_{sat} (squares) and $E_\perp$ (circles) probe signals 2.5 cm into the SOL of an L-mode discharge using I_{sat} as the reference signal, revealing well-defined, correlated peaks, and (b) the normalized (to 2.5× rms level) I_{sat} signal at various radial locations from the LCFS in the SOL showing peak broadening due to a "tail." The threshold used for width calculation is shown as a horizontal dashed line at I_{sat} ~1.5 rms.

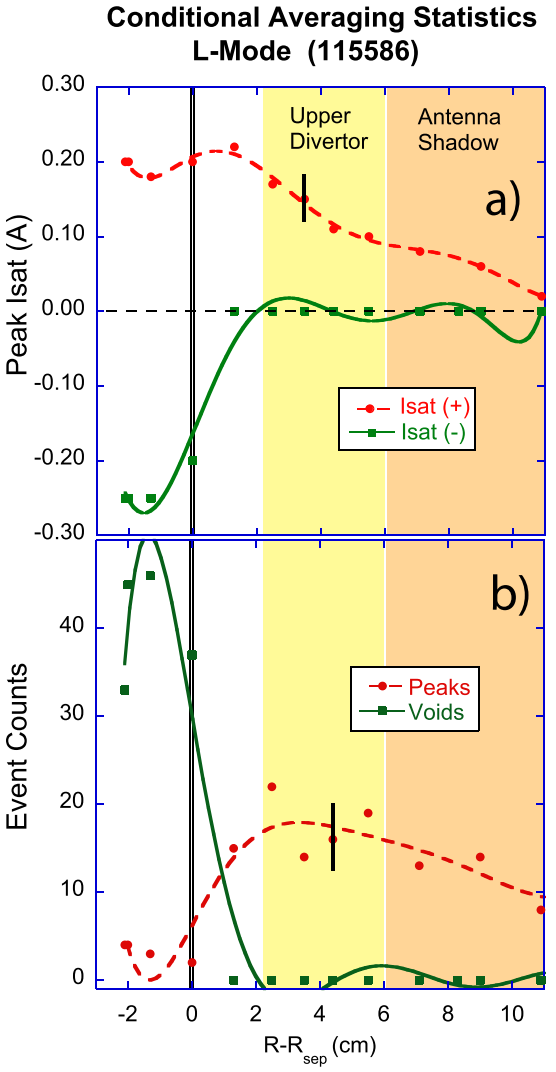

FIG. 11. Radial profiles of, (a) amplitude of the intermittent I_{sat}peaks (I_{sat+}, circles) and voids (I_{sat-}, squares) and (b) number of peak or voids events (circles, squares) are shown. A polynomial fit is done to guide the eye. The probe is more closely connected to the active (lower) divertor in the near SOL, further out the field lines are also closely connected to the upper divertor, and in the far SOL, to the antennae structure inside the vessel. We have marked these regions in the plots.

negative I_{sat} events is largest inside the LCFS and it is clear the voids only exist at and inside the LCFS where only few peaks (~5) are detectable, indicating that peak-void separation occurs at the LCFS in these discharges. The positive peak's amplitude decays monotonically throughout the SOL, as they are drained by parallel transport, even at short connection lengths to various vessel structures thus highlighting the relevance of convective transport. The question of continuity and particle conservation, and why the number of positive and negative events are not the same at/near the LCFS, comes to mind. The answer is complex and nonlinear because, among other effects, like dissipation and shear fragmentation, filaments that are too large or too small to be stable are expected to disintegrate due to Rayleigh-Taylor, Kelvin-Helmholtz, and other instabilities.[82,85,86]

We can extract the perpendicular (to $\vec{B}$) velocity of the plasma using cross-correlation techniques of time-delay estimation between tips separated by ~4 mm in the perpendicular direction and assuming the turbulence is moving with the plasma. The plasma velocity profile, shown in Fig. 12(a), indicates a velocity of 10 km/s in the electron diamagnetic direction (EED) in the core and LCFS (solid line is a spline fit to guide the eye only) and a much lower velocity of up 2 km/s in the ion diamagnetic direction (IDD) in the SOL, resulting in a ~1 cm thin shear layer featuring a shear rate of $\omega_s \approx 1 \times 10^6\ s^{-1}$ which will tend to stabilize modes and breakup turbulent eddies. We can compare that to a filament autocorrelation time of $\tau_c \approx 2 \times 10^{-5}$ s extracted from Fig. 10, assuming a dominant convective transport mechanism. In short, the plasma is near stabilizing turbulence already in L-mode.

The radial velocity profile of the intermittent events, show in Fig. 12(b), is calculated as $V_r = E_\perp \times B/B^2$ where $E_\perp$ is the peak value obtained from CA over 5 ms and B is the value of the local magnetic field at the probe location (~0.24 T). Two sets of points are shown: (1) the outward velocity of the intermittent peaks as open circles, fairly flat at 3–5 km/s and (2) the inward velocity of the voids as filled squares, at up to −6 km/s inside the LCFS. The voids do not exist in the SOL, therefore a velocity of zero has been

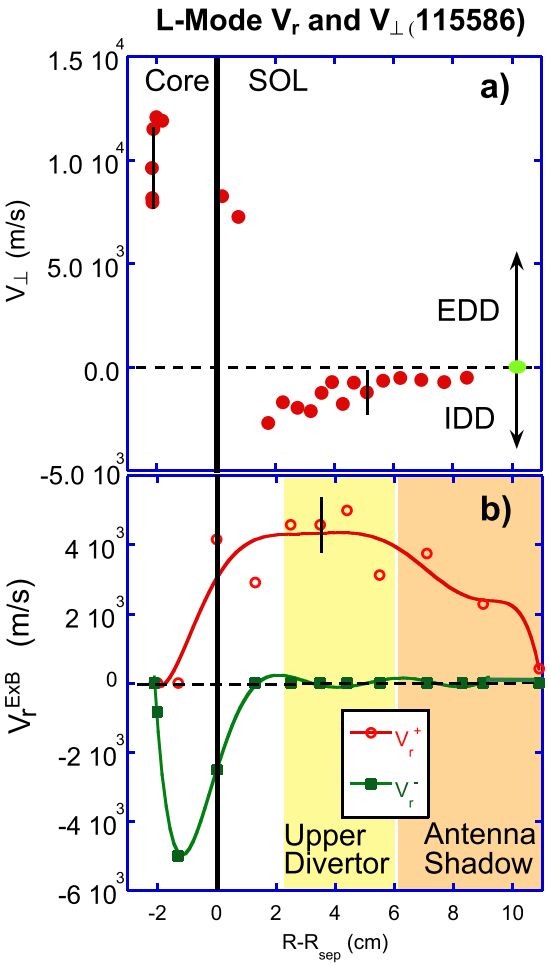

FIG. 12. Profiles of (a) $V_\perp$ velocity extracted from time-delay cross-correlation and (b) radial $[V_r = (\vec{E}_\perp \times \vec{B})/B^2]$ velocity of the positive events/peaks (open circles) and negative events/voids (solid squares) obtained from conditional averaging. The EDD and IDD are indicated as well as the location of vessel structures.

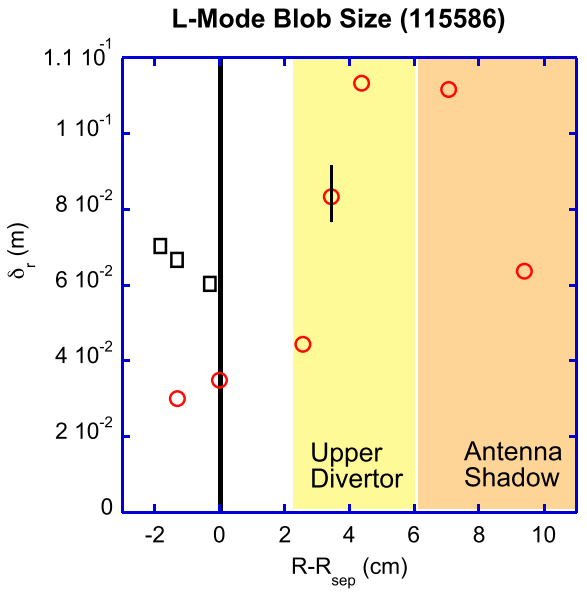

FIG. 13. Average filament radial size/diameter profile (circles) obtained from conditional averaging using the CA radial velocity and event duration $\partial r = V_r \times \partial t$ and poloidal size (squares) by using the dominant perpendicular velocity $\partial\theta = V_\perp \times \partial t$ at/near the LCFS.

arbitrarily assigned in that region and a polynomial fit to the data is shown only to guide the eye.

The ***average*** size of the filaments, $\partial r, \partial\perp$, or diameter if symmetry is assumed at the LCFS, is estimated[31] as $\partial x = V_x \times \partial t$ (where $x = r, \perp$) if we know V_x and the filament transit time, ∂t, over the probe tips. In the SOL, the assumption $V_r \gg V_\perp$ can be used, whereas at/inside the LCFS $V_\perp \approx 2V_r$ is true, as seen in Fig. 12(a). The filament transit time is estimated using the full-width, half-max, (FWHM) of the conditionally averaged I_{sat} pulses [Figs. 10(a) and 10(b)], which become longer and asymmetric, developing a tail,[84–86] shown in Fig. 10(b), as they propagate into the SOL. The filament size estimate, in this case the diameter, if we assume that the filaments are fairly symmetric in the $\perp$, r plane, starts at ~6–7 cm in the core and increases to 8–10 cm in the SOL, as shown in Fig. 13. The circles are inferred from $\partial r = V_r \times \partial t$ (inside the LCFS we use the negative velocity from the voids), and the squares from $\partial\perp = V_\perp \times \partial t$ the calculated filament diameter (theoreticians commonly use the filament radius,[7,93] not the diameter) is dependent on how the filament transit time is defined, and we use the half-height-full-width (HHFW) criteria, measured at the horizontal dashed line in Fig. 10(b).

For comparison to former results and those of other devices, the filaments in NSTX can be placed in an electrostatic instability regime parameter space, as described in Ref. 93 in terms of dimensionless collisionality, and filament scale size, defined in terms of electron-ion collision frequency, υ_{ei}, parallel connection length. $L_\parallel$ electron gyrofrequency, Ω_e, ion gyroradius, ρ_s, magnetic field, B, major radius, R, and filament radius, a_b, as[92]

$$\Lambda = \nu_e L_\parallel / \Omega_e \rho_s = 1.7 \times 10^{-14}\, n_e L_\parallel / T_e^2, \qquad (2)$$

$$\hat{a} = a_b R^{1/5} / L_\parallel^{2/5} \rho_s^{4/5} = 0.018 a_b B^{4/5} R^{1/5} / L_\parallel^{2/5} T_e^{2/5}. \qquad (3)$$

The $\Lambda - \hat{a}^{5/2}$ non-dimensional space, computed for the geometrical factors, $\varepsilon_x = 0.3$ and $f = 3.3$, i.e., distortion factors due to fanning effects in the X-point region, treated in detail by Myra,[93] contains several filament/blob regimes, as shown in Fig. 14 and labeled as: connected ideal interchange (CI), connected sheath-interchange (CS), resistive X-point (RX), and resistive ballooning (RB). Additionally, we can estimate if the boundary is in a regime where electromagnetic effects are important by evaluating the parameter α_{MHD}, given by

$$\alpha_{MHD} = L_\parallel^2 \beta / R\, a_b = 2.2 \times 10^{-11} L_\parallel^2 T_e n_e / R\, a_b B^2, \qquad (4)$$

which yields $\alpha_{MHD} \sim 3.1$ in L-mode, indicating that blob propagation drive is a competition between ideal MHD and Alfvénic line bending effects.[89,90]

The filament/blob parameters for the L-mode at NSTX result in values of $\Lambda \sim 0.54/0.39$ and $\hat{a} \sim 1.21/4.5$ for the LCFS/SOL, respectively, which are plotted as circles in Fig. 14, and of $\Lambda = 0.13/0.02$ and $\hat{a} = 0.6/1.25$ in H-mode, which are plotted as stars in Fig. 14. The LCFS parameters fall in the boundary between the CI and RX regimes, while

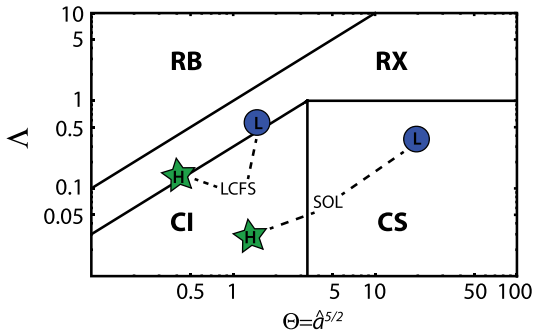

FIG. 14. The filament parameters in L-mode (circles) and H-mode (stars) are shown in the $\Lambda - \hat{a}^{5/2}$ non-dimensional space indicating the various regimes. The LCFS parameters fall along the boundary between CI and RX regime while the SOL parameters fall well in the connected (sheath and interchange) CS-CI regimes. The LCFS values are not far from the RB regime.

the SOL parameters fall well in the connected interchange/sheath (CI-CS) regimes. Identifying the instability regimes is important since then predictions on growth rates and filament velocity can be made and compared to data. In the CI and CS regimes, the filament velocity varies as $\hat{V} \approx \varepsilon_x \hat{a}^{1/2}$, $\hat{V} \approx 1/\hat{a}^2$, respectively. A detailed treatment of this issue will be addressed in future work since it requires a parameter scan, thus outside the scope of this paper.

III. DISCUSSION

The observed profiles of fluctuations and radial particle transport (Fig. 6) peaking at the LCFS are not commonly documented, but often observed in tokamaks and consistent with often-used transport coefficients in edge fluid codes. In NSTX, it is notable that the electric filed, $\tilde{E}_\perp$, fluctuations increase monotonically towards the core as the flux $\tilde{\Gamma}_r$ decreases sharply, indicating that it is the density fluctuations $\tilde{n}$ and $\tilde{n} - \tilde{E}_\perp$ cross-phase effects that determine the inward shape of the flux profile. It is also notable that there is a hint of an inward pinch, which is often invoked in simulations to obtain the experimental profiles.

The skewness profiles shown in Fig. 9 reflect the presence of voids at or inside $\Psi_n \approx 0.95$ due to both intermittency and ELMs, as in the H-mode case we include roughly 2–3 ELMs in the 5 ms time series. However, the skewness is positive further out, reflecting the plasma filaments and ELMs that propagate into the SOL. The skewness of the flux is compounded by the skewness of both the density and electric field skewness and also the cross-phase between them.

To place these results in a general framework, the location of the filaments in the $\Lambda - \hat{a}^{5/2}$ non-dimensional space is similar to previous GPI-based observations for NSTX and Alcator C-Mod.[93] Radial velocities are in a similar range of 1–5 km/s and although the filament size is larger in NSTX than in DIII-D, the normalized values (to ρ_S) are fairly comparable.

Inspection of Figs. 5 and 6 show that plasma presence in the SOL and transport in H-mode is drastically reduced from L-mode levels, this occurs in all discharges, and should be reflected in the intermittency. Since conditional averaging of the chosen H-mode discharges (Fig. 1) is complicated by the presence of type III ELMs, we have chosen another discharge (115517) with a brief ELM-free period, which often occurs right after the L-H transition and that can be used to evaluate the characteristics of the intermittency during the H-mode as well as changes induced by the transition. The probe remained at a roughly constant position of $R - R_{sep} = 2.9$ cm (i.e., in the near-mid SOL) during the L-H transition, so all the changes, shown in Fig. 15, are purely due to the evolving L-H transition physics. We have used 4 ms time series.

Upon the L-H transition, the number of filaments [Fig. 15(a)] drops only slightly on average with some oscillations due to some breakup of filaments by the increased

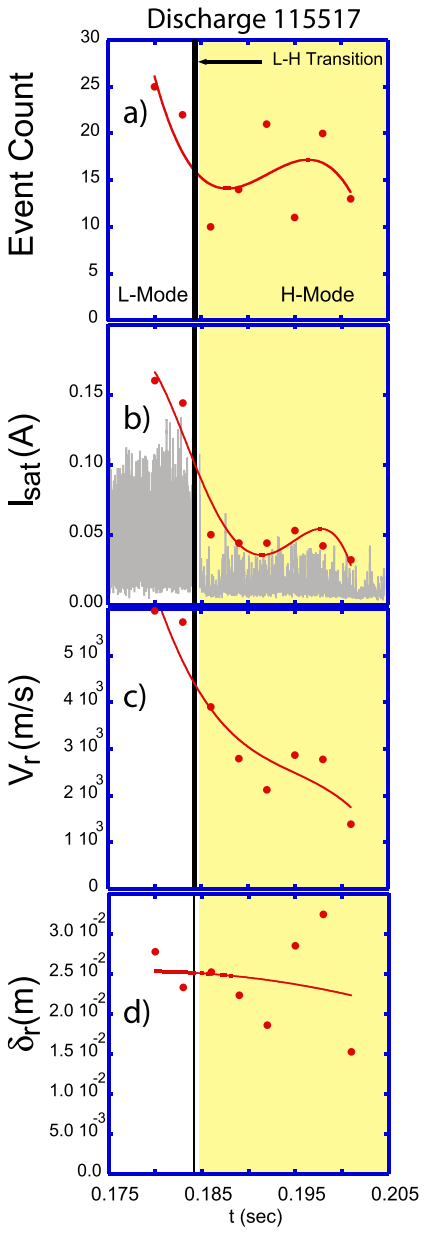

FIG. 15. Comparison of filament characteristics from conditional averaging at a fixed location, $R - R_{sep} = 2.9$ cm, during a L-H transition. We plot, (a) number of events slightly dropping on average, (b) amplitude of I_{sat-} (raw signal in background overlay) is reduced by a factor of 3, (c) radial velocity, V_r, drops by a factor of 3 while (d), filament size/diameter, ∂_r, remains roughly constant at ~2.5–3 cm.

poloidal velocity shear inside the LCFS.[59] The most drastic changes occur on the filament's I_{sat} (i.e., $\propto n_e\sqrt{T_e}$) and radial velocity V_r, [Figs. 15(b) and 15(c)] that drop by a factor of 3. In the absence of a fast T_e measurement, relative contribution of T_e and n_e can not be assessed although parallel conductivity is known to reduce T_e rapidly. Since $V_r \approx V_\perp$ at $\sim$2.5 km/s in the SOL, then filament size, ∂r, remains roughly constant at 2.5–3 cm $(a_b \sim 1.5)$, as long as we assume $\partial_r \approx \partial_\perp$, i.e., roughly symmetric filaments. An explanation for the strong reduction in I_{sat} and V_r upon transition to H-mode can be that the stronger H-mode sheared flows can momentarily trap the filaments while they lose heat and particles, and release them at lower velocity,[59] this is definitely a topic for further study and intrinsically related to the details of the L-H transition and shear layer dynamics. It is noteworthy that the number of filaments >2.5 rms selected by the CA technique, and their diameter remain roughly constant after the L-H transition while the broadband turbulence and smaller filaments [seen in the I_{sat} overlay in Fig. 15(b)] which are not selected by CA may suffer stronger suppression.

We can put the present results in context of existing results obtained in NSTX via imaging techniques with high temporal resolution using a GPI system[47,48,92,94] and photomultiplier arrays. The probe results presented here and earlier imaging results are, in general, in good agreement. Imaging of the intermittent structures permits dynamics visualization and quantitative measurements of velocity, poloidal, and radial extent, etc. It is clear that the intermittent objects are born from edge turbulence inside or at the LCFS[9,47,48,58] and that both broadband turbulence and intermittent objects are substantially reduced (meaning amplitude, velocity, or both) during H-mode with respect to the Ohmic or L-mode regimes.[9,24,31,65]

Quantitative comparison between probe and imaging results indicates some small differences which can be attributed to different functional dependencies on the fluctuating $n_e$and T_e between diagnostics, to different analysis methods applied on the raw data, and to variations in the phenomena studied between the discharges used in the different published works. These quantitative discrepancies are typically not greater than factors 2 or 3. For example, recent imaging work puts the radial velocity of the filaments near the LCFS in the range 0.2–1.5 km/s, and filament size, a_b, is about 1–2 cm (Ref. 93) in L-mode discharges while the probe measures a_b of 2.5–5 cm and velocities <0.2 km/s inside the LCFS rising to 3–5 km/s in the SOL. Notice that the filament size varies significantly as the analysis probe data for the L-H transition in discharge 115517 show $a_b \sim 1.5$ cm and V_r of 2 km/s.

Early GPI measurements of individual blob velocities in NSTX[47] showed a range of −4 to 4 km/s in the poloidal direction and of −2 to 2 km/s in the radial direction while later measurements[48] showed radial profiles with time-averaged poloidal turbulence velocity profiles in the range of 2–8 km/s (Ref. 92) in L-mode in the IDD. Flows in the electron diamagnetic directions (EDD) inside the LCFS are generally seen in the imaging data[94–96] at least qualitatively similar to the present probe data. The GPI camera data also allow the determination of poloidal and radial correlation lengths (4–9 cm and 2–6 cm, respectively)[48,92] in rough agreement with the probe results. The relative fluctuation level of GPI emission, due to density and temperature fluctuations, increases from the LCFS towards SOL,[91] similarly to the observations from probe data. A recent review[97] showing a database of filament velocity and size shows a very large spread in filament radius from 0.5–4 cm and poloidal filament velocity 0–4 km/s. A robust comparison of diagnostic results is difficult since the velocity scaling with size varies tremendously with blob regime, and as shown in Fig. 14, a filament can cross from one regime to another while moving into the SOL, therefore comparison is only possible in carefully planned experiments with overlapping discharges and locations.

IV. SUMMARY

Measurements with probes in the edge plasma of NSTX in L and H-mode discharges show that the plasma can extend far into the SOL, most notably in L-mode, above the expected exponential decay, resulting in significant particle and (at least convected) heat fluxes to wall structures, as seen in other tokamaks. We characterize for the first time the turbulent radial particle transport in the edge and SOL of NSTX, showing it peaks at the LCFS at $\sim 5 \times 10^{21} S^{-1} m^{-2}$ in L-mode, dropping by a factor of 8–10 in H-mode. The H-mode flux can fully account for the global particle transport as determined by SOLPS modeling performed for the same discharges, but in L-mode, a ballooning-like poloidal asymmetry in transport is required. The particle transport profile shape, which features a slight pinch inside the LCFS, is chiefly determined by density fluctuations and $\tilde{n} - \tilde{E}_\perp$ cross phase effects, the latter more dominant in H-mode. The ***normalized rms*** density and potential fluctuations vary from 10%–20% inside the LCFS to up to $\sim$100% in the SOL. Plasma filaments/blobs and voids appear as intermittent fluctuations at a rate of $10^3 - 10^4\ s^{-1}$ at the LCFS. Statistical measurements, such as skewness, indicating non-Gaussian events, are confirmed by conditional averaging, and reveal that voids move inward at 2–5 km/s, whereas peaks propagate outward at 3–5 km/s while their amplitude and number decay with radius. Filament size/diameter in L-mode can be estimated at 5–10 cm, larger than in DIII-D, and they can spread as they develop a tail while propagating into the SOL, consistent with predicted internal potential structures that produce shear flows and can interact with the background and also create internal KH and interchange instabilities. Despite apparent differences between NSTX filament parameters and those in other tokamaks, they all fall in fairly similar electrostatic instability regimes (namely boundary CL-RX and CS regimes) that determine different velocity scaling. Upon transition to H-mode, the filament density and radial velocity are reduced by factor $\sim$3 in the near SOL while size and numbers drop only slightly, reflecting the effect of reduced turbulence source and velocity shear. These measurements motivate the need for more experiments for cross-diagnostic comparison (probe-GPI, etc) in identical

conditions and to address the physics of blob generation and sheared flow-blob interaction.

ACKNOWLEDGMENTS

This work was supported in part by the U.S. Department of Energy under DE-FG02-07ER54917, DE-AC02-09CH11466, DE-AC52-07NA27344, DE-AC05-00OR22725, and DE-FG02-08ER54984.

[1]Ch. P. Ritz, R. V. Bravenec, P. M. Schoch, R. D. Bengtson, J. A. Boedo, J. C. Forster, K. W. Gentle, Y. He, R. L. Hickok, Y.-J. Kim, H. Lin, P. E. Phillips, T. L. Rodes, W. L. Rowan, P. M. Valanju, and A. J. Wootton, Phys. Rev. Lett. **62**, 1844 (1989).
[2]S. J. Zweben and R. W. Gould, Nucl. Fusion **25**, 171 (1985).
[3]Ch. P. Ritz, R. V. Bravenec, R. D. Bengtson, K. W. Gentle, C. C. Klepper, P. E. Phillips, E. J. Powers, T. L. Rhodes, B. Richards, W. L. Rowan, and A. J. Wootton, J. Nucl. Mater. **145–147**, 241 (1987).
[4]H. Biglari, P. H. Diamond, and P. W. Terry, Phys. Fluids B **2**, 1 (1990).
[5]F. Wagner, G. Becker, K. Behringer, D. Campbell, A. Eberhagen, W. Engelhardt, G. Fussmann, O. Gehre, J. Gernhardt, G. v. Glerke, G. Hass, M. Huang, F. Karger, M. Keilhacker, O. Klueber, M. Kornherr, K. Lackner, G. Lisitano, G. G. Lister, H. M. Mayer, D. Meisel, E. R. Mueller, H. Murmann, H. Niedermayer, W. Poschenrieder, H. Rapp, H. Roehr, F. Schneider, G. Siller, E. Speth, A. Staebler, K. H. Steuer, G. Yenus, O. Vollmer, and Z. Yue, Phys. Rev. Lett. **49**(19), 1408 (1982).
[6]B. LaBombard, R. L. Boivin, M. Greenwald, J. Hughes, B. Lipschultz, D. Mossessian, C. S. Pitcher, J. L. Terry, and S. J. Zweben, and Alcator Group, Phys. Plasmas **8**, 2107 (2001).
[7]S. I. Krasheninnikov, Phys. Lett. A **283**, 368 (2001).
[8]S. J. Zweben, Phys. Fluids **28**, 974 (1985).
[9]J. A. Boedo, D. Rudakov, R. Moyer, S. Krasheninnikov, D. Whyte, G. McKee, G. Tynan, M. Schaffer, P. Stangeby, W. West, S. Allen, T. Evans, R. Fonck, E. Hollmann, A. Leonard, A. Mahdavi, G. Porter, M. Tillack, and G. Antar, Phys. Plasmas **8**, 4826 (2001).
[10]D. D'Ippolito, J. R. Myra, and S. I. Krasheninnikov, Phys. Plasmas **9**, 222 (2002).
[11]A. H. Nielsen, H. L. Pécseli, and J. Juul Rasmussen, Phys. Plasmas **3**, 1530 (1996).
[12]R. D. Lehmer, Ph.D. thesis, University of California, Los Angeles, UCSDENG-032, 1996.
[13]E. Sanchez, C. Hidalgo, D. López-Bruna, I. García-Cortés, R. Balbín, M. A. Pedrosa, B. van Milligen, C. Riccardi, G. Chiodini, J. Bleuel, M. Endler, B. A. Carreras, and D. E. Newman, Phys. Plasmas **7**, 1408 (2000).
[14]J. F. Lyon, B. A. Carreras, K. K. Chipley, M. J. Cole, J. H. Harris, T. C. Jernigan, R. L. Johnson, and R. L. Lynch, Fusion Technol. **10**, 179 (1986).
[15]I. Garcia-Cortes, M. A. Pedrosa, C. Hidalgo, B. Branas, T. Estrada, R. Balbin, E. de la Luna, J. Sanchez, and A. P. Navarro, Phys. Fluids B **4**, 4007 (1992).
[16]I. Garcia-Cortes, R. Balbín, A. Loarte, J. Bleuel, A. Chankin, S. J. Davies, M. Endler, S. K. Erents, C. Hidalgo, G. F. Matthews, B. van Milligen, and H. Thomsen, Plasma Phys. Controlled Fusion **42**, 389 (2000).
[17]B. K. Joseph, R. Jha, P. K. Kaw, S. K. Mattoo, C. V. S. Rao, and Y. C. Sazena, Phys. Plasmas **4**, 4292 (1997).
[18]C. Hidalgo, Plasma Phys. Controlled Fusion **37**, A53 (1995).
[19]R. Jha and Y. C. Saxena, Phys. Plasmas **3**, 2979 (1996).
[20]A. V. Filippas, R. D. Bengston, G.-X. Li, M. Meier, Ch. P. Ritz, and E. J. Powers, Phys. Plasmas **2**, 839 (1995).
[21]M. V. Umansky, S. I. Krasheninnikov, B. LaBombard, and J. L. Terry, Phys. Plasmas **5**, 3373 (1998).
[22]B. LaBombard, M. V. Umansy, R. L. Boivin, J. A. Goetz, J. Hughes, B. Lipschultz, D. Mossessian, C. S. Pitcher, J. L. Terry, and Alcator Group, Nucl. Fusion **40**, 2041 (2000).
[23]J. L. Terry, S. J. Zweben, K. Hallatschek, B. LaBombard, R. J. Maqueda, B. Bai, C. J. Boswell, M. Greenwald, D. Kopon, W. M. Nevins, C. S. Pitcher, B. N. Rogers, D. P. Stotler, and X. Q. Xu, Phys. Plasmas **10**, 1739 (2003).
[24]S. J. Zweben, D. P. Stotler, J. L. Terry, B. LaBombard, M. Greenwald, M. Muterspaugh, C. S. Pitcher, K. Hallatschek, R. J. Maqueda, B. Rogers, J. L. Lowrance, V. J. Mastrocola, and G. F. Renda, Phys. Plasmas **9**, 1981 (2002).
[25]O. E. Garcia, S. M. Fritzner, and R. Kube, Phys. Plasmas **20**, 055901 (2013).
[26]J. G. Watkins, R. A. Moyer, D. N. Hill, D. Buchenauer, T. N. Carlstrom, R. Conn, J. Cuthbertson, R. Doerner, R. Lehmer, M. A. Mahdavi, R. T. McGrath, L. Schmitz, and R. D. Stambaugh, J. Nucl. Mater. **196–198**, 829 (1992).
[27]M. R. Wade, W. A. Houlberg, L. R. Baylor, W. P. West, and D. R. Baker, Phys. Rev. Lett. **84**, 282 (2000).
[28]D. L. Rudakov, J. A. Boedo, R. A. Moyer, P. C. Stangeby, J. G. Watkins, D. G. Whyte, L. Zeng, N. H. Brooks, R. P. Doerner, T. E. Evans, M. E. Fenstermacher, M. Groth, E. M. Hollmann, S. Krasheninnikov, C. J. Lasnier, A. W. Leonard, M. A. Mahdavi, G. R. McKee, A. G. McLean, A. Y. Pigarov, W. R. Wampler, G. Wang, W. P. West, and C. P. C. Wong, Nucl. Fusion **45**, 1589 (2005).
[29]D. L. Rudakov, J. A. Boedo, R. A. Moyer, S. Krasheninnikov, A. W. Leonard, M. A. Mahdavi, G. R. McKee, G. D. Porter, P. C. Stangeby, J. G. Watkins, W. P. West, D. G. Whyte, and G. Antar, Plasma Phys. Controlled Fusion **44**, 717 (2002).
[30]J. A. Boedo, D. L. Rudakov, R. J. Colchin, R. A. Moyer, S. Krasheninnikov, D. G. Whyte, G. R. McKee, M. J. Schaffer, P. C. Stangeby, W. P. West, S. L. Allen, and A. W. Leonard, J. Nucl. Mater. **313–316**, 813 (2003).
[31]J. A. Boedo, D. L. Rudakov, R. A. Moyer, G. R. McKee, R. J. Colchin, M. J. Schaffer, P. G. Stangeby, W. P. West, S. L. Allen, T. E. Evans, R. J. Fonck, E. M. Hollmann, S. Krasheninnikov, A. W. Leonard, W. Nevins, M. A. Mahdavi, G. D. Porter, G. R. Tynan, D. G. Whyte, and X. Xu, Phys. Plasmas **10**, 1670 (2003).
[32]M. E. Fenstermacher, A. W. Leonard, P. B. Snyder, J. A. Boedo, N. H. Brooks, R. J. Colchin, D. S. Gray, R. J. Groebner, M. Groth, E. Hollmann, C. J. Lasnier, T. H. Osborne, T. W. Petrie, D. L. Rudakov, H. Takahashi, J. G. Watkins, L. Zeng, and DIII-D Team, Plasma Phys. Controlled Fusion **45**, 1597 (2003).
[33]N. Asakura, Y. Koide, K. Itami, N. Hosogane, K. Shimizu, S. Tauji-Iio, and S. Sakurai, J. Nucl. Mater. **241–243**, 559 (1997).
[34]N. Asakura, M. Takechi, N. Oyama, and T. Nakano, J. Nucl. Mater. **337–339**, 712 (2005).
[35]M. Endler, H. Niedermeyer, L. Giannone, E. Kolzhauer, A. Rudyj, G. Theimer, and N. Tsois, Nucl. Fusion **35**, 1307 (1995).
[36]J. Neuhauser, D. Coster, H. U. Fahrbach, J. C. Fuchs, G. Haas, A. Herrmann, L. Horton, M. Jakobi, A. Kallenbach, M. Laux, J. W. Kim, B. Kurzan, H. W. Müller, H. Murmann, R. Neu, V. Rohde, W. Sandmann, W. Suttrop, E. Wolfrum, and ASDEX Upgrade Team, Plasma Phys. Controlled Fusion **44**, 869 (2002).
[37]A. Kallenbach, R. Dux, J. Gafert, G. Haas, L. D. Horton, M. Jakobi, B. Kurzan, H. W. Müller, R. Neu, J. Neuhauser, R. Pugno, T. Pütterich, V. Rohde, W. Sandmann, S.-W. Yoon, and ASDEX Upgrade Team, Nucl. Fusion **43**, 573 (2003).
[38]A. Herrmann, T. Eich, V. Rohde, C. J. Fuchs, J. Neuhauser, and ASDEX Upgrade Team, Plasma Phys. Controlled Fusion **46**, 971 (2004).
[39]Ph. Ghendrih, Y. Sarazin, M. Becoulet, G. Huysmans, S. Benkadda, P. Beyer, C. Figarella, X. Garbet, P. Monier-Garbet, and JET Team, J. Nucl. Mater. **313–316**, 914 (2003).
[40]B. Goncalves, C. Hidalgo, M. A. Pedrosa, C. Silva, R. Balbin, K. Erents, M. Hron, A. Loarte, and G. Matthews, Plasma Phys. Controlled Fusion **45**, 1627 (2003).
[41]W. Fundamenski, W. Sailor, and JET EFDA Contributors, Plasma Phys. Controlled Fusion **46**, 233 (2004).
[42]M. Endler, I. Garcia-Cortes, C. Hidalgo, G. F. Matthews, ASDEX Team, and JET Team, Plasma Phys. Controlled Fusion **47**, 219 (2005).
[43]M. V. A. P. Heller, Z. A. Brasilio, I. L. Caldas, J. Söckel, and J. Petrzilka, Phys. Plasmas **6**, 846 (1999).
[44]J. P. Graves, J. Horacek, R. A. Pitts and K. I. Hopcraft, Plasma Phys. Contr. Fusion **47**, L1 (2005).
[45]O. E. Garcia, R. A. Pitts, J. Horacek, A. H. Nielsen, W. Fundamenski, J. P. Graves, V. Naulin, and J. J. Rasmussen, J. Nucl. Mater. **363**, 575 (2007).
[46]O. E. Garcia, J. Horacek, R A. Pitts, A. H. Nielsen, W. Fundamenski, V. Naulin, and J. J. Rasmussen, Nucl. Fusion. **47**, 667 (2007).
[47]R. J. Maqueda, G. A. Wurden, D. P. Stotler, S. J. Zweben, B. LaBombard, J. L. Terry, J. L. Lowrance, V. J. Mastrocola, G. F. Renda, D. A. D'Ippolito, J. R. Myra, and N. Nishino, Rev. Sci. Instrum. **74**, 2020 (2003).
[48]S. J. Zweben, R. J. Maqueda, D. P. Stotler, A. Keesee, J. Boedo, C. E. Bush, S. M. Kaye, B. LeBlanc, J. L. Lowrance, V. J. Mastrocola, R. Maingi, N. Nishino, G. Renda, D. W. Swain, J. B. Wilgen, and NSTX Team, Nucl. Fusion **44**, 134 (2004).
[49]Y. Yang, G. F. Counsell, and MAST Team, J. Nucl. Mater. **313–316**, 734 (2003).

[50]G. Y. Antar, G. F. Counsell, and J.-W. Ahn, Phys. Plasmas **12**, 082503 (2005).
[51]B. A. Carreras, V. E. Lynch, D. E. Newman, R. Balbin, J. Bleuel, M. A. Pedrosa, M. Endler, B. van Milligen, E. Sánchez, and C. Hidalgo, Phys. Plasmas **7**, 3278 (2000).
[52]B. A. Carreras, V. E. Lynch, and B. LaBombard, Phys. Plasmas **8**, 3702 (2001).
[53]B. A. Carreras, C. Hidalgo, E. Sanchez, M. A. Pedrosa, R. Balbín, I. García-Cortés, B. van Milligen, D. E. Newman, and V. E. Lynch, Phys. Plasmas **3**, 2664 (1996).
[54]H. E. Roman, C. Riccardi, and S. Magni, Journal of Physics: Conference Series **7**, 239–246 (2005).
[55]A. V. Nedospasov, J. Nucl. Mater. **196–198**, 90–100 (1992).
[56]Y. Sarazin, V. Grandgirard, E. Fleurence, X. Garbet, P. Ghendrih, P. Bertrand, and G. Depret, Plasma Phys. Controlled Fusion **47**, 1817 (2005).
[57]Y. Sarazin and Ph. Ghendrih, Phys. Plasmas **5**, 4214 (1998).
[58]B. Lipschultz, D. Whyte, and B. LaBombard, Plasma Phys. Controlled Fusion **47**, 1559 (2005).
[59]D. A. Russell, J. R. Myra, and D. A. D'Ippolito, Phys. Plasmas **16**, 122304 (2009).
[60]A. Y. Pigarov, S. I. Krasheninnikov, T. D. Rognlien, M. J. Schaffer, and W. P. West, Phys. Plasmas **9**, 1287 (2002).
[61]A. Y. Pigarov, S. I. Krasheninnikov, W. P. West, T. D. Rognlien, J. A. Boedo, D. G. Whyte, C. J. Lasnier, T. W. Petrie, M. J. Schaffer, and J. G. Watkins, J. Nucl. Mater. **313–316**, 1076 (2003).
[62]G. R. McKee, R. Ashley, R. Durst, R. Fonck, M. Jakubowski, K. Tritz, K. Burrell, C. Greenfield, and J. Robinson, Rev. Sci. Instrum. **70**, 913 (1999).
[63]J. W. Connor, R. J. Hastie, H. R. Wilson, and R. L. Miller, Phys. Plasmas **5**, 2687 (1998).
[64]P. B. Snyder, H. R. Wilson, J. R. Ferron, L. L. Lao, A. W. Leonard, T. H. Osborne, A. D. Turnbull, D. Mossessian, M. Murakami, and X. Q. Xu, Phys. Plasmas **9**, 2037 (2002).
[65]J. A. Boedo, D. L. Rudakov, E. Hollmann, D. S. Gray, K. H. Burrell, R. A. Moyer, G. R. McKee, R. Fonck, P. C. Stangeby, T. E. Evans, P. B. Snyder, A. W. Leonard, M. A. Mahdavi, M. J. Schaffer, W. P. West, M. E. Fenstermacher, M. Groth, S. L. Allen, C. Lasnier, G. D. Porter, N. S. Wolf, R. J. Colchin, L. Zeng, G. Wang, J. G. Watkins, and T. Takahash, Phys. Plasmas **12**, 072516 (2005).
[66]A. W. Leonard, J. A. Boedo, M. Groth, B. L. Lipschultz, G. D. Porter, D. L. Rudakov, and D. G. Whyte, J. Nucl. Mater. **363–365**, 1066 (2007).
[67]D. Rudakov, J. Boedo, R. Moyer, N. Brooks, R. Doerner, *et al.*, J. Nucl. Mater. **337–339**, 717–721 (2005).
[68]T. E. Evans, R. A. Moyer, J. G. Watkins, T. H. Osborne, P. R. Thomas, M. Becoulet, J. A. Boedo, E. J. Doyle, M. E. Fenstermacher, K. H. Finken, R. J. Groebner, M. Groth, J. H. Harris, G. L. Jackson, R. J. La Haye, C. J. Lasnier, S. Masuzaki, N. Ohyabu, D. G. Pretty, H. Reimerdes, T. L. Rhodes, D. L. Rudakov, M. J. Schaffer, M. R. Wade, G. Wang, W. P. West, and L. Zeng, Nucl. Fusion **45**, 595 (2005).
[69]J. A. Boedo, N. Crocker, and L. Chousal, Rev. Sci. Instrum. **80**, 123506 (2009).
[70]P. H. Diamond and T. S. Hahm, Phys. Plasmas **2**, 3640 (1995).
[71]J. Menard, private communication (2009).
[72]L. L. Lao, H. E. St. John, R. D. Stambaugh, A. G. Kellman, and W. Pfeiffer, Nucl. Fusion **25**, 1611 (1985).
[73]S. A. Sabbagh, S. M. Kaye, J. Menard, F. Papletti, M. Bell, R. E. Bell, J. M. Bialek, M. Bitter E. D. Fredrickson, D A. Gates A. H. Glasser, H. Kugel, L. L. Lao, B. P. LeBlanc, R. Maingi, R. J. Mazzucato, D. Mueller, M. Ono, S. F. Paul, M. Peng, C. H. Skinner, D. Stutman, G. A. Wurden, W. Zhu, and NSTX Research Team, Nucl. Fusion **41**, 1601 (2001).
[74]J. A. Boedo, D. S. Gray, P. W. Terry, S. Jachmich, G. R. Tynan, R. W. Conn, and TEXTOR-94 Team, Nucl. Fusion **42**, 117 (2002).
[75]M. G. Shats, K. Toi, K. Ohkuni, Y. Yoshimura1, M. Osakabe, G. Matsunaga, M. Isobe, S. Nishimura, S. Okamura, K. Matsuoka, and CHS Group, Phys. Rev. Lett. **84**, 6042 (2000).
[76]R. Schneider, X. Bonnin, K. Borrass, D. P. Coster, H. Kastelewicz, D. Reiter, V. A. Rozhansky, and B. J. Braams, Contrib. Plasma Phys. **46**, 3 (2006).
[77]B. J. Braams, Contrib. Plasma Phys. **36**, 276 (1996).
[78]D. Reiter, M. Baelmans, and P. Boerner, Fusion Sci. Technol. **47**, 172 (2005).
[79]J. M. Canik, R. Maingi, V. A. Soukhanovskii, R. E. Bell, H. W. Kugel, B. P. LeBSlanc, and T. H. Osborne, J. Nucl. Mater. **415**, S409 (2011).
[80]G. R. Tynan, L. Schmitz, R. W. Conn, R. Doerner, and R. Lehmer. Phys. Rev. Lett. **68**, 3032 (1992).
[81]V. A. Soukhanovskii, R. E. Bell, C. Bush, R. Kaita, H. W. Kugel, B. P. LeBlanc, R. Maingi, R. Raman, A. L. Roquemore, and NSTX Research Team, J. Nucl. Mater. **390–391**, 516 (2009).
[82]N. Bian, S. Benkadda, J.-V. Paulsen, and O. E. Garcia, Phys. Plasmas **10**, 671 (2003).
[83]Y. Sarazin, Ph. Ghendrih, G. Attuel, C. Clément, X. Garbt, C. Grandgirad, M. Ottcini, A. Benkadda, P. Beyer, N. Bian, and C. Figarella, J. Nucl. Mater. **313–316**, 796 (2003).
[84]G. Q. Yu and S. I. Krasheninnikov, Phys. Plasmas **10**, 4413 (2003).
[85]D. A. D'Ippolito, J. R. Myra, S. I. Krasheninnikocv, G. Q. Yu, and A. Yu. Pigarov, Contrib. Plasma Phys. **44**, 205 (2004).
[86]O. E. Garcia, N. H. Bian, and W. Fundamenski, Phys. Plasmas **13**, 082309 (2006).
[87]X. Q. Xu, W. M. Nevins, T. D. Rognlien, R. H. Bulmer, M. Greenwald, A. Mahdavi, L. D. Pearlstein, and P. Snyder, Phys. Plasmas **10**, 1773 (2003).
[88]D. A. Russell, D. A. D'Ippolito, J. R. Myra, W. M. Nevins, and X. Q. Xu, Phys. Rev. Lett. **93**, 265001 (2004).
[89]J. Myra and D. A. D'Ippolito, Phys. Plasmas **12**, 092511 (2005).
[90]S. I. Krasheninnikov, D. D. Ryutov, and G. Yu, J. Plasma Fusion Res. **6**, 139 (2004).
[91]J. Zweben, R. J. Maqueda, R. Hager, K. Hallatschek, S. M. Kaye, T. Munsat, F. M. Poli, A. L. Roquemore, Y. Sechrest, and D. P. Stotler, Phys. Plasmas **17**, 102502 (2010).
[92]S. J. Zweben, R. J. Maqueda, J. L. Terry, T. Munsat, J. R. Myra, D. D'Ippolito, D. A. Russell, J. A. Krommes, B. LeBlanc, T. Stoltzfus-Dueck, D. P. Stotler, K. M. Williams, C. E. Bush, R. Maingi, O. Grulke, S. A. Sabbagh, and A. E. White, Phys. Plasmas **13**, 56114 (2006).
[93]J. R. Myra, D. A. D'Ippolito, D. P. Stotler, S. J. Zweben, B. P. LeBlanc, J. E. Menard, R. J. Maqueda, and J. Boedo, Phys. Plasmas **13**, 092509 (2006).
[94]Y. Sechrest, T. Munsat, D. A. D'Ippolito, R. J. Maqueda, J. R. Myra, D. Russell, and S. J. Zweben, Phys. Plasmas **18**, 012502 (2011).
[95]J. R. Myra, W. M. Davis, D. A. D'Ippolito, B. LaBombard, D. A. Russell, J. L. Terry, and S. J. Zweben, Nucl. Fusion **53**, 073013 (2013).
[96]R. J. Maqueda, D. P. Stotler, and NSTX Team, Nucl. Fusion **50**, 075002 (2010).
[97]D. A. D'Ippolito, J. R. Myra, and S. J. Zweben, Phys. Plasmas **18**, 060501 (2011).